

Evidence of anisotropic bulk superconductivity in disorder-induced ZrTe_{3-x}

P. Manna,¹ C. Patra,¹ T. Agarwal,¹ S. Srivastava,¹ S. Sharma,¹ P. Mishra,¹ and R. P. Singh^{1,*}

¹*Department of Physics, Indian Institute of Science Education and Research Bhopal, Bhopal, 462066, India*

Transition-metal trichalcogenides distinguish themselves from other two-dimensional materials in nanoscience and materials science due to their remarkable range of intrinsic properties, including various electronic, optical, and magnetic behaviors. Here, we report a comprehensive study of superconductivity in disordered ZrTe_{3-x} ($x = 0.2$) with suppressed charge density wave. We observe a type-II bulk anisotropic superconductivity with a superconducting transition at $T_c = 3.59(4)$ K. Angle-dependent upper critical field measurements and Berezinskii-Kosterlitz-Thouless transition confirm the inherent quasi-two-dimensional nature of superconductivity in this disordered system.

I. INTRODUCTION

The complex interplay between charge density waves (CDWs) and superconductivity, characterized by competing [1, 2] and coexisting [3], has posed intriguing questions in condensed matter physics. These correlated phenomena are mainly caused by Fermi-surface instabilities and electron-phonon interactions [4]. In the weak-coupling regime, they often compete for the same electronic states, so that introducing disorder can suppress one order while simultaneously enhancing the other [5, 6]. While this interplay has gained significant traction through studies of cuprate superconductors [1, 7, 8], it is equally prevalent in transition-metal trichalcogenides and layered transition-metal dichalcogenides [9, 10].

Group IVB transition-metal trichalcogenides (TMTCs), distinguished by their strongly anisotropic crystal structures, form a notable subclass of two-dimensional (2D) materials [11]. Their unique combination of structural and electronic features makes them ideal candidates for exploring emergent physical phenomena, particularly in addressing the long-standing puzzle surrounding the interplay between dimensionality and superconductivity. They additionally offer remarkable quasi-one-dimensional (quasi-1D) characteristics, which combine the advantages of 2D materials with promising platforms for fabricating nanoelectronic devices and probing new avenues in nanotechnology. Different compositions of binary zirconium tellurium compounds have garnered significant research interest due to their intriguing properties, including negative magnetoresistance [12, 13], quantum Hall effect [14], log-periodic oscillations [15], and potential topological characteristics [16, 17].

In this context, the CDW compound ZrTe_3 [18] is of particular interest due to its unusual coexistence of filamentary and bulk superconductivity [19]. ZrTe_3 crystallizes in the TaSe_3 -type structure with the space group $\text{P}2_1/\text{m}$ (11). Along the b direction, it consists of an infinite quasi-1D chain, whereas quasi-2D Zr-Te layers are formed along the ac -plane [20]. Pristine ZrTe_3 undergoes a CDW transition around 63 K, driven by Fermi surface

nesting [18] with filamentary superconductivity emerging only below 2 K [21]. While bulk superconductivity can be induced via elemental substitution, atomic intercalation, disorder tuning, or the application of external pressure [22–28], these methods often obscure intrinsic electronic properties, and the exact nature of superconductivity remains elusive. Recent research demonstrates that suppressing the CDW state via controlled disorder can induce robust bulk superconductivity with an enhanced transition temperature (T_c), providing a clearer avenue for probing the fundamental physics of quasi-2D superconducting systems [29–33].

Here, we report the successful synthesis of crystalline ZrTe_{3-x} ($x = 0.2$) and comprehensive characterization of its superconducting properties via magnetization, specific heat, and transport measurements. The results confirm anisotropic type-II superconductivity with $T_c = 3.59(4)$ K and complete suppression of the CDW state. Furthermore, angle-dependent magnetotransport and clear signatures of a Berezinskii-Kosterlitz-Thouless (BKT) transition provide compelling evidence for quasi-two-dimensional superconductivity in bulk single crystals of ZrTe_{3-x} ($x = 0.2$).

II. EXPERIMENTAL DETAILS

$\text{ZrTe}_{2.8}$ single-crystals were grown employing the typical isothermal chemical vapor transport (ICVT) method, with iodine (I_2) chunks serving as the transport agent. Zr (5N) lumps and finely powdered Te (4N) pieces were combined in accurate stoichiometric proportions and sealed in an evacuated quartz tube along with I_2 (5mg/cc). The tube was then placed in a box furnace and kept at a constant temperature of 900 K. After a 10-day reaction time, the system was cooled in ice-water and large shiny crystals formed. The identity and phase purity of the crystals were examined using powder X-ray diffraction (PXRD) applying monochromatic $\text{Cu}-K\alpha$ radiation ($\lambda = 1.54$ Å) on an X'pert PANalytical Empyrean X-ray diffractometer, and the Laue diffraction pattern was obtained using a Photonic Science Laue camera. Elemental compositions were confirmed by energy-dispersive X-ray analysis (EDAX) in combination with scanning electron microscopy (SEM). Magnetization measurements were

* rpsingh@iiserb.ac.in

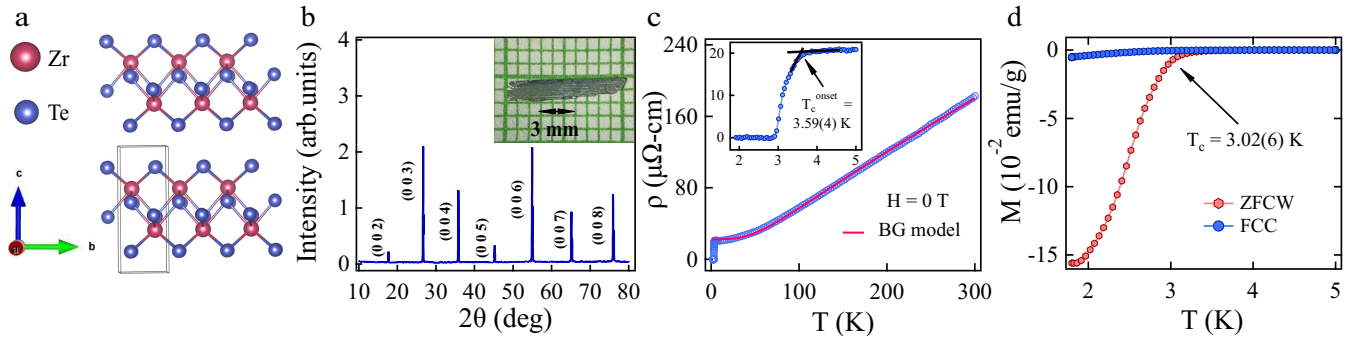


FIG. 1. (a) The crystal structure of $\text{ZrTe}_{2.8}$ is shown, where the pink and blue spheres stand in for the Zr and Te atoms, respectively. (b) Distinct $(00l)$ reflections are visible in single-crystal XRD patterns, suggesting a preferential orientation along the c -axis. Inset: Crystal image taken with an optical microscope. (c) A magnified view of the resistivity near the superconducting transition reveals an onset transition temperature of approximately $3.59(4)$ K. Inset: The temperature-dependent electrical resistivity conducted in zero magnetic field is fitted with the BG model. (d) Magnetization versus temperature measurements under a very low applied field display a broad superconducting transition with a critical temperature of $3.02(6)$ K.

performed on a Quantum Design magnetic property measurement system (MPMS3) equipped with a cryostat ^4He . A 9T-Quantum Design physical property measuring system (PPMS) was introduced to carry out transport and specific heat measurements using conventional four-probe and two-tau methods, respectively.

III. RESULTS AND DISCUSSION

a. Sample characterization

Fig. 1(a) displays the crystal structure of $\text{ZrTe}_{2.8}$ along the a -axis, produced by VESTA software [34]. The room-temperature powder X-ray diffraction patterns of the crushed crystal of $\text{ZrTe}_{2.8}$ were analyzed using the Rietveld refinement [35], shown in (a), which confirms a single phase present in Te-deficient ZrTe_{3-x} . This compound has a monoclinic structure with space group $\text{P}2_1/\text{m}$ (11). The lattice parameters obtained from the refinement are $a = 5.9052(7)$ Å, $b = 3.9492(6)$ Å, $c = 10.1121(5)$ Å, which are slightly higher than the parent compound. The inset of Fig. 1(b) shows the microscopic image of a 1 cm long silver-colored crystal. The single crystal XRD patterns of $\text{ZrTe}_{2.8}$ are illustrated in Fig. 1(b), where the crystals are oriented along the $(00l)$ direction, implying the c -axis as a growth axis. The Laue diffraction pattern (Left inset of S1(b), Supplemental Material [36]) confirms the crystallinity of the sample, while the EDAX analysis verifies the intended elemental compositions (see Fig. S1(b), Supplemental Material [36]).

b. Electrical resistivity and Magnetization

The temperature-dependent AC electrical resistivity of the crystalline $\text{ZrTe}_{2.8}$ was measured from 1.9 K to 300 K in the absence of an external magnetic field, as illustrated

in Fig. 1(c). The gradual decrease in resistivity from 300 K to 5 K reflects the metallic behavior of the compound, with a residual resistivity ratio (RRR), $\rho(300\text{K})/\rho(5\text{K})$, of roughly 9, indicative of relatively low scattering from defects or impurities in the crystal. A broad superconducting transition is observed at low temperatures: the onset of superconductivity begins at a higher temperature of $3.59(4)$ K, while the resistivity drops to zero at $2.86(2)$ K, as illustrated schematically in the inset of Fig. 1(c). Interestingly, no resistivity anomaly is observed near 63 K, where a charge density wave (CDW) transition would normally be expected as the parent compound. It suggests suppression of the CDW phase, likely due to Te deficiency, which can weaken the nesting condition necessary for CDW formation. The normal-state resistivity is well described by the Bloch-Grüneisen (BG) model, which captures the temperature dependence of electron-phonon scattering. This model is expressed as

$$\rho(T) = \rho_0 + \rho_{BG}(T). \quad (1)$$

Where, $\rho_{BG}(T)$, the temperature-dependent contribution of BG is defined as

$$\rho_{BG}(T) = r \left(\frac{T}{\theta_D} \right)^3 \int_0^{\theta_D/T} \frac{x^3}{(e^x - 1)(1 - e^{-x})} dx. \quad (2)$$

ρ_0 represents the temperature-independent residual resistivity, r is a material-dependent constant, and θ_D denotes the Debye temperature. The fitting parameters are estimated as $\rho_0 = 22.5(4)$ $\mu\Omega\text{-cm}$ and the Debye temperature $\theta_D = 366(1)$ K.

Temperature-dependent magnetization measurements offer crucial evidence for identifying bulk superconductivity. These measurements were carried out using two standard protocols: zero-field-cooled warming (ZFCW) and field-cooled cooling (FCC), under an applied magnetic field of 1 mT. The superconducting transition temperature is typically determined from the bifurcation point of the ZFCW and FCC curves, as illustrated in Fig. 1(d).

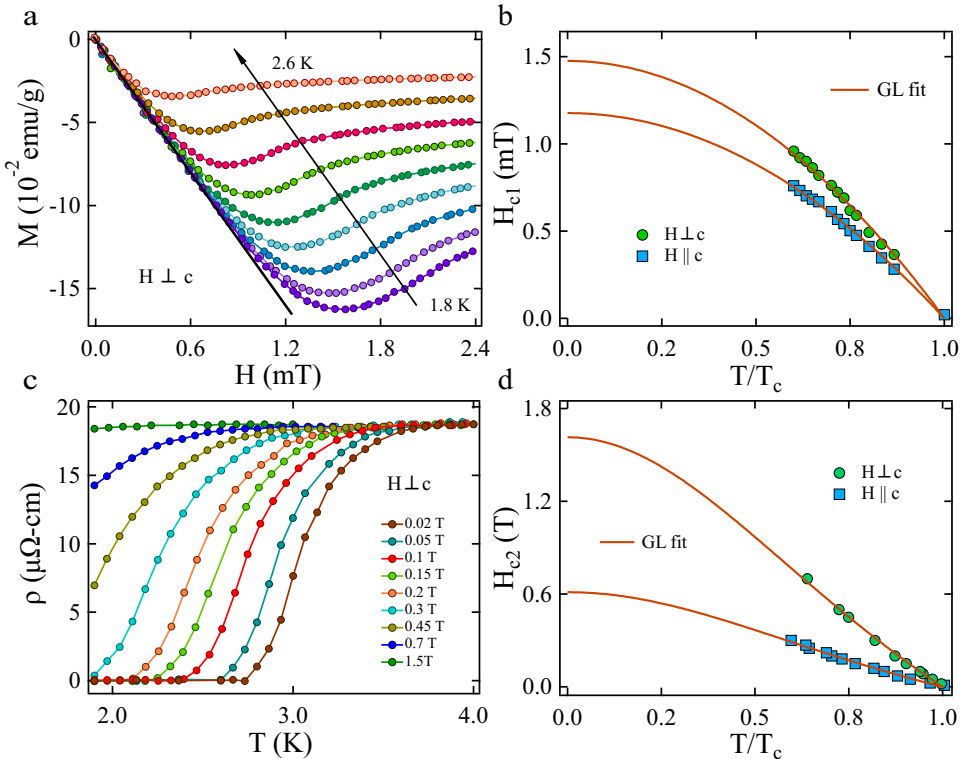


FIG. 2. (a) Field-dependent magnetization curves at various temperatures for H perpendicular to c -axis is shown. (b) Temperature-dependent lower critical fields in both directions. GL-fitting is shown by the orange lines. (c) Temperature-dependent electrical resistivity for magnetic fields applied parallel to the ab plane. (d) The conventional GL model is used to fit upper critical fields in both orientations as a function of reduced temperature, represented by orange solid lines.

A distinct diamagnetic response observed in both modes confirms the onset of bulk superconductivity at 3.02(6) K. The comparatively weaker magnetization signal in the FCC mode relative to the ZFCW mode is likely due to strong flux pinning effects within the sample.

To determine the lower critical field $H_{c1}(0)$, field-dependent magnetization measurements were performed on a range of fixed temperatures. The H_{c1} values were identified from the magnetization curves (M) versus the magnetic field (H) at the point where the data begin to deviate from the initial linear region, corresponding to the Meissner effect. This deviation marks the onset of magnetic flux penetration into the sample, signaling the lower critical field. As shown in Fig. 2(a) and S2(a) (Supplemental Material [36]), these measurements were

performed for two configurations: with the magnetic field perpendicular and parallel to the crystallographic c -axis, respectively. The extracted $H_{c1}(T)$ values were then analyzed as a function of reduced temperature employing the typical Ginzburg-Landau (GL) relation described as

$$H_{c1}(T) = H_{c1}(0) [1 - t^2], \quad \text{where } t = \frac{T}{T_c} \quad (3)$$

which gives $H_{c1}(0) = 1.17(6)$ and $1.47(5)$ mT for H parallel to the c -axis and H perpendicular to the c -axis, respectively, as given in Fig. 2(b). Temperature-dependent resistivity measurements were conducted under various externally applied magnetic fields to evaluate the upper critical field ($H_{c2}(0)$), as presented in Fig. 2(c) and S2(b) (Supplemental Material [36]) for magnetic fields aligned parallel and perpendicular to the same plane, respectively. The increase in the magnetic field leads to a systematic decrease in the superconducting transition temperature (T_c). We adopted a commonly used criterion based on the decrease in resistivity, where the transition point is defined as $\rho = 0.9\rho_n$, with ρ_n denoting the resistivity of the normal state just above the transition. The resulting extrapolated $H_{c2}(T)$ data were then examined using the standard GL framework (Eq. (4)) that enables the

TABLE I. The anisotropic superconducting parameters.

Parameters	Unit	$H \parallel c$	$H \perp c$
$H_{c1}(0)$	mT	1.17(6)	1.47(5)
$H_{c2}^{res}(0)$	T	0.61(2)	1.61(4)
ξ	nm	8.82(1)	23.2(4)
λ_{GL}	nm	620.2(2)	689.0(4)
κ_{GL}		29.7	45.7

extrapolation of $H_{c2}(0)$.

$$H_{c2}(T) = H_{c2}(0) \left[\frac{1-t^2}{1+t^2} \right], \quad \text{where } t = \frac{T}{T_c}. \quad (4)$$

So, the estimated values of $H_{c2}(0)$ are 0.61(2) and 1.61(4) T for $H \parallel c$ and $H \perp c$, respectively (Fig. 2(d)). These fits not only provide the zero-temperature limit of H_{c2} for both orientations, but also provide insight into the anisotropic nature of superconductivity, which can be quantified by calculating the anisotropic parameter $\Gamma = H_{c2}^{\parallel c}/H_{c2}^{\perp c}$ as 0.38. The moderate anisotropy observed in this system is consistent with the quasi-two-dimensional character of the superconducting state, as expected from layered structural motifs. A comparative overview of anisotropy parameters across bulk and monolayer superconductors is summarized in S2(d). This quasi-2D behavior is further supported by the angle-dependent upper critical field measurements, which reinforce the presence of anisotropic superconducting properties.

The Pauli limiting mechanism and the orbital limiting effect are two fundamental factors that predominantly govern the destruction of superconductivity in the presence of an external magnetic field. The Pauli limiting effect involves Zeeman splitting, which breaks Cooper pairs by aligning electron spins in the same direction. In contrast, the orbital limiting effect, originating from the Lorentz force, disrupts the coherent motion of Cooper pairs through the induction of vortices. Following the BCS theory, the Pauli limit effect is calculated as 6.67(7) T using $H_{c2}^P(0) = 1.86 T_c$ with $T_c = 3.59(4)$ K [37, 38]. This value lies above the experimentally determined in-plane upper critical field, inferring that the Pauli limit is preserved. Additionally, the orbital limiting effect is assessed using the Werthamer-Helfand-Hohenberg (WHH) theory, applicable to type-II superconductors under the assumption of negligible spin-orbit coupling [39, 40]. It is defined as

$$H_{c2}^{orb}(0) = -\alpha T_c \left. \frac{dH_{c2}(T)}{dT} \right|_{T=T_c}. \quad (5)$$

Here, α is a dimensionless constant referred to as the purity factor, which distinguishes between superconductors of the clean and dirty limit, taking values of 0.73 and 0.69 for superconductors of the clean and dirty limit, respectively. The estimated value of $H_{c2}^{orb}(0)$ is 0.92(1) T for $\alpha = 0.69$. Since the upper critical field values for both in-plane and out-of-plane orientations lie well below the Pauli limit, this signifies the role of the orbital effect.

In anisotropic superconductors, the relationship between the superconducting coherence length (ξ) and the upper critical field (H_{c2}) is quantitatively described by a well-established theoretical model [41], as follows:

$$H_{c2} = \frac{\phi_0}{2\pi\xi_{\perp c}^2} (\cos^2\theta + \epsilon^2 \sin^2\theta)^{-1/2}. \quad (6)$$

Here $\phi_0 = h/2e$ is the magnetic flux quanta, with a value of 2.07×10^{-15} Tm². The parameter ϵ is the anisotropy ratio

between the two coherence lengths along the in-plane and out-of-plane directions, defined as $\epsilon = \xi_{\parallel c}/\xi_{\perp c}$. θ refers to the angle between the direction of the applied magnetic field and the unit vector normal to the superconducting layers. By evaluating the general expression for the angular dependence of the upper critical field [Eq. (6)] in the limiting cases of $\theta = 0^\circ$ and 90° , we arrive at simplified formulas for the coherence lengths in the parallel and perpendicular directions relative to the field. Specifically, for $\theta = 0^\circ$, the upper critical field is given by $H_{c2}^{\parallel}(0) = \frac{\phi_0}{2\pi\xi_{\perp}^2}$, and for $\theta = 90^\circ$, it is $H_{c2}^{\perp}(0) = \frac{\phi_0}{2\pi\xi_{\parallel}\xi_{\perp}}$. So, using these relations, we calculate the coherence lengths to be $\xi_{\parallel c} = 8.82(1)$ nm and $\xi_{\perp c} = 23.2(4)$ nm, respectively.

A series of usual theoretical relations are applied to acquire the GL-penetration length (λ) and the GL parameter (κ): $H_{c2}^{\perp}(0)/H_{c1}^{\perp}(0) = 2\kappa_{\perp c}^2/\ln\kappa_{\perp c}$, $\kappa_{\perp c} = [\lambda_{\perp c}(0)\lambda_{\parallel c}(0)/\xi_{\perp c}(0)\xi_{\parallel c}(0)]^{1/2}$, and $\kappa_{\parallel c} = \lambda_{\perp c}(0)/\xi_{\perp c}(0)$. The complete set of extracted superconducting parameters is listed in Table I. The calculated values of κ for both orientations significantly exceed the critical threshold of $1/\sqrt{2}$, thereby unambiguously confirming that ZrTe_{2.8} belongs to the class of strong type-II superconductors. Moreover, the thermodynamic critical field (H_c), which serves as a measure of the superconducting condensation energy, was found to be around 0.024(8) T, with $H_c(0) = H_{c1}^{\perp}(0)\sqrt{2}\kappa_{\perp c}/\ln\kappa_{\perp c}$. Table II lists the superconducting parameters of other Zr-based superconductors.

c. Specific heat

The occurrence of the superconducting transition is further supported by a pronounced discontinuity in the zero-field-specific heat data, which affirms the presence of bulk superconductivity in this layered material. The system undergoes a second-order phase transition at 2.7 K, which closely matches the values T_c identified in the resistivity and magnetization measurements. To analyze the behavior of the normal-state, the specific heat data above the transition were fitted using the Debye-Sommerfeld model, expressed as $C(T) = \gamma_n T + \beta_3 T^3$, where the first term represents the electronic contribution to the heat capacity, governed by the Sommerfeld coefficient γ_n , and the second term accounts for the phononic (lattice) contri-

TABLE II. Superconducting parameters of ZrTe_{2.8} with other Zr-based compounds.

Compounds	T_c (K)	$H \parallel c$ (T)	$H \perp c$ (T)	Γ
ZrTe _{3-x}	3.59	0.61	1.61	0.38
ZrTe _{3-x}				
nanoplates	3.4	0.5	2.5	0.2
Cu _{0.05} ZrTe ₃	3.8	1.3	3.2	0.41
Ni _{0.05} ZrTe ₃	3.1	0.48	1.23	0.39

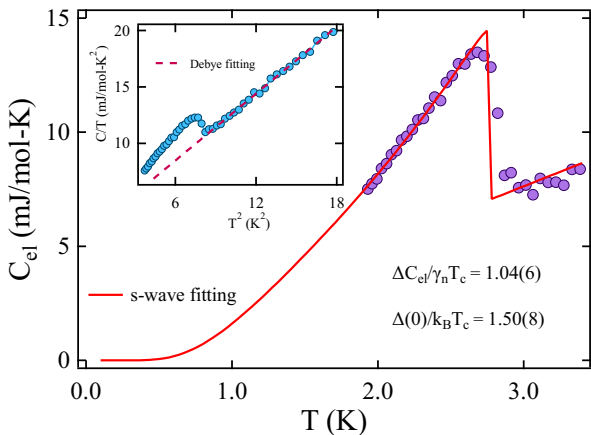


FIG. 3. Electronic specific heat is fitted with an isotropic s-wave model, supporting conventional superconducting behavior. Inset: Debye-Sommerfeld model fit to the normal-state specific heat data.

bution at low temperatures through the Debye constant β_3 . This fitting, illustrated in the inset of Fig. 3, yields the parameters $\gamma_n = 2.54(3)$ mJ mol⁻¹ K⁻² and $\beta_3 = 0.98(8)$ mJ mol⁻¹ K⁻⁴. The extracted value β_3 was then used to calculate the Debye temperature θ_D , which provides valuable information about the phonon spectrum and vibrational dynamics of the crystal lattice. The Debye temperature is determined using the following relation:

$$\theta_D = \left(\frac{12\pi^4 RN}{5\beta_3} \right)^{\frac{1}{3}}, \quad (7)$$

where $R = 8.314$ J mol⁻¹ K⁻¹ is the universal gas constant, and $N = 4$ corresponds to the number of atoms per formula unit. The obtained Debye temperature, θ_D , is found to be approximately 195.98(2) K, which is slightly lower than the value obtained from the fit of BG to the resistivity in the normal state. This discrepancy likely arises from the use of different temperature ranges in the respective analyzes.

In BCS-type superconductors, the electronic density of states at the Fermi level, $N(E_F)$, is a fundamental parameter that significantly influences the superconducting pairing mechanism. It governs the availability of electronic states that participate in the formation of Cooper pairs. This quantity can be estimated by incorporating γ_n in $\gamma_n = \left(\frac{\pi^2 k_B^2}{3} \right) N(E_F)$, where $k_B = 1.38 \times 10^{-23}$ J K⁻¹. The resulting value of $N(E_F)$ is 1.80(6) states eV⁻¹f.u.⁻¹. The modified McMillan equation [42] is used to evaluate the electron-phonon coupling constant, λ_{e-ph} , which measures the strength of the interaction between electrons and lattice vibrations (phonons). It is written as follows:

$$\lambda_{e-ph} = \frac{1.04 + \mu^* \ln(\theta_D/1.45T_c)}{(1 - 0.62\mu^*) \ln(\theta_D/1.45T_c) - 1.04}; \quad (8)$$

where μ^* represents the Coulomb pseudopotential, which accounts for electron-electron repulsion and is generally assumed to be 0.13 for transition metal-based superconductors. Applying this formalism with $T_c = 3.59(4)$ K and $\theta_D = 195.46(1)$ K, the result λ_{e-ph} is 0.61(9). This value indicates that the compound studied belongs to the category of weakly coupled BCS superconductors.

Important information about the underlying pairing mechanism of the superconducting state may be gained from the temperature dependence of the electron-specific heat data. To isolate the electronic contribution, the phononic part of the zero-field specific heat is deducted using the formula $C_{el} = C - \beta_3 T^3$, where β_3 is the lattice contribution extracted from the normal-state fit. The resulting data C_{el} are analyzed using a single-gap s-wave BCS model [43], as shown in Fig. 3. Entropy S can be assessed using this paradigm, as

$$\frac{S}{\gamma_n T_c} = -\frac{6}{\pi^2} \left(\frac{\Delta(0)}{k_B T_c} \right) \int_0^\infty [f \ln(f) + (1-f) \ln(1-f)] dy, \quad (9)$$

where, $f(\xi) = [e^{\beta E(\xi)} + 1]^{-1}$ is the Fermi-Dirac distribution function, where $\beta = 1/k_B T$ and $E(\xi) = \sqrt{\xi^2 + \Delta^2(t)}$ is the quasiparticle excitation energy. The variable ξ denotes the energy of normal-state electrons measured relative to the Fermi level, while $\Delta(t)$ is the superconducting energy gap as a function of the reduced temperature $t = T/T_c$. For the purpose of integration, the variable substitution $y = \xi/\Delta(0)$ is applied. The temperature-dependent superconducting gap is described by the empirical formula: $\Delta(t) = \tanh[1.82(1.018[(1/t) - 1])^{0.51}]$, implementing the isotropic s-wave BCS approximation. The electronic specific heat is then related to the entropy via the thermodynamic relation $C_{el}(T) = t \frac{dS}{dt}$. By fitting the experimental data $C_{el}(T)$ using this formalism, the superconducting gap ratio $\Delta(0)/k_B T_c$ is determined to be approximately 1.50(8), which is in excellent agreement with the prediction of BCS for weak-coupling superconductors. Furthermore, the specific heat jump at T_c , denoted as $\Delta C_{el}/\gamma_n T_c$, is found to be nearly 1.04(6), further supporting the classification of this material as a conventional s-wave superconductor.

d. Two-dimensional superconductivity

Angle-dependent upper critical field: The angle-dependent upper critical field is a useful probe for identifying anisotropy and possible two-dimensional superconducting behavior. To investigate this, field-dependent resistivity measurements were performed at a stable temperature of 2 K for various angles, as shown in Fig. 4(a), where θ is defined as the angle between the applied magnetic field and the normal to the sample plane, with the current always along the *ab* plane. The upper critical field at each angle was extracted using the criterion $\rho = 0.9\rho_n$,

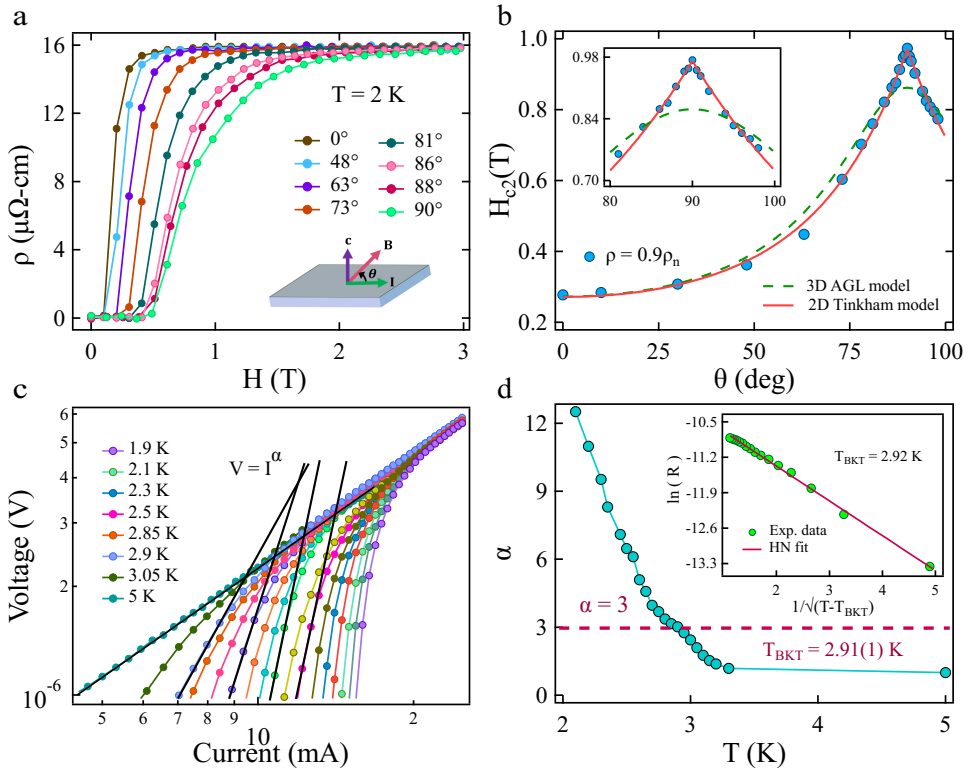


FIG. 4. (a) Field-dependent electrical resistivity with different angles supports an anisotropic nature of this compound. Inset: Schematic of a tilt experimental setup. (b) Angle-dependent upper critical fields $\rho = 0.9\rho_n$ are best portrayed by the two-dimensional Tinkham model over the three-dimensional anisotropic GL model. Inset: expanded view of the fitting near 90° angle. (c) The temperature-dependent current-voltage (V - I) curves at zero magnetic field are plotted on a logarithmic scale. (d) The exponent (α) values from power-law fitting correspond to the BKT transition temperature at $2.91(1)$ K. The slope of $\alpha(T) = 3$ is marked by the horizontal dotted line. Inset: The Halperin-Nelson fitting is also incorporated to calculate the BKT transition temperature, indicating T_{BKT} at 2.92 K.

where ρ_n is the resistivity in the normal state. As shown in Fig. 4(b), the angular dependence of H_{c2} displays a pronounced cusp near $\theta = 90^\circ$, which becomes more apparent in the magnified view provided in the inset. Such a sharp angular feature is a hallmark of strong anisotropy and often suggests the presence of quasi-two-dimensional superconductivity. Two theoretical models are commonly considered to explain the angular dependence of H_{c2} . The anisotropic Ginzburg–Landau (AGL) model (Eq. (10)) describes the angular variation for three-dimensional superconductors, resulting in an ellipsoidal form of $H_{c2}(\theta)$. In contrast, Tinkham’s model (Eq. (11)) captures the behavior in two-dimensional thin-film superconductors and predicts a characteristic cusp at $\theta = 90^\circ$. Comparing the experimental data with these models allows us to assess the dimensionality and anisotropy of the superconducting state in this system.

$$\left(\frac{H_{c2}(\theta, T) \sin \theta}{H_{c2}^\perp}\right)^2 + \left(\frac{H_{c2}(\theta, T) \cos \theta}{H_{c2}^\parallel}\right)^2 = 1 \quad (10)$$

$$\left(\frac{H_{c2}(\theta, T) \sin \theta}{H_{c2}^\perp}\right)^2 + \left|\frac{H_{c2}(\theta, T) \cos \theta}{H_{c2}^\parallel}\right| = 1 \quad (11)$$

The experimental data are better described by the two-dimensional Tinkham model than by the three-dimensional AGL model [30], indicating a more pronounced two-dimensional nature of superconductivity. Collectively, these results suggest that the superconductivity in $\text{ZrTe}_{2.8}$ exhibits a quasi-two-dimensional behavior.

Berezinskii-Kosterlitz-Thouless (BKT) transition: In addition to angle-dependent upper critical field measurements, a powerful complementary approach to probe the two-dimensional nature of superconductivity is through the identification of a Berezinskii-Kosterlitz-Thouless (BKT) transition in the transport behavior of ZrTe_{3-x} . In contrast to three-dimensional superconductors, which can support true long-range phase coherence, two-dimensional superconductors are limited to exhibiting quasi-long-range order due to enhanced thermal fluctuations. The BKT transition emerges as the system transitions from a quasi-long-range ordered vortex–antivortex phase to a fully disordered state with increasing temperature [44]. The temperature-dependent current-voltage characteristics (V - I) (as plotted in Fig. 4(c)) are used to extract the BKT transition temperature, T_{BKT} . Below T_c , the application of high currents can break the

vortex-antivortex pairs, resulting in a non-ohmic response. In this regime, the V - I characteristic nicely follows a power-law dependence (Eq. (12)), where the exponent is directly proportional to the superfluid density (J_s). The equilibrium density of the free vortices $n_v(I)$ scales as a power of the applied current, which is the typical origin of the behavior mentioned above. Consequently, the voltage response behaves as $V \propto n_v(I)I$, capturing the nonlinear dynamics of the vortex motion in the quasi-2D superconducting state [45]. In the ideal scenario of a BKT transition, it is predicted that the superfluid density J_s exhibits a universal and discontinuous jump at the critical temperature where it intersects the BKT line. When this behavior is substituted for Eq. (12), it implies that the voltage-current exponent should also show an abrupt change at the transition point, which serves as a hallmark of the BKT mechanism.

$$V \propto I^{\alpha(T)}, \quad \alpha(T) = 1 + \pi \frac{J_s(T)}{T}. \quad (12)$$

$$J_s(T_{BKT}^-) = \frac{2}{\pi T_{BKT}}, \quad J_s(T_{BKT}^+) = 0. \quad (13)$$

$$\alpha(T_{BKT}^-) = 3, \quad \alpha(T_{BKT}^+) = 1. \quad (14)$$

By fitting the power-law dependence described by Eq. (12), we extracted the temperature-dependent exponent $\alpha(T)$, as shown in Fig. 4(d). The extracted α increases with decreasing temperature and approaches a value of 3 near 2.91(1) K, which is identified as T_{BKT} .

Additionally, to check the consistency of the BKT behavior, another theoretical approach proposed by Halperin and Nelson is used. According to the Halperin-Nelson equation (HN), in the temperature range just above T_{BKT} , the resistance follows an exponential dependence given by Eq. (15).

$$R = R_0 \exp\left[\frac{-b}{(T - T_{BKT})^{1/2}}\right]. \quad (15)$$

Here, R_0 is a material-specific constant, and b tells about the strength of the vortex-antivortex interaction. This expression is valid within a narrow temperature window above T_{BKT} , where superconductivity is suppressed by phase fluctuations induced by thermal unbinding of vortex-antivortex pairs. The plot of $\ln R$ versus $1/(T - T_{BKT})^{1/2}$ is linearly fitted to estimate T_{BKT} (Inset of Fig. 4(d)). Yielded value of T_{BKT} is 2.92 K, which aligns well with the estimate obtained from the non-linear I - V power-law analysis.

The agreement between these two independent methods, nonlinear scaling V - I and Halperin-Nelson fitting, strongly supports the presence of a Berezinskii-Kosterlitz-Thouless transition, reinforcing the quasi-two-dimensional nature of superconductivity in this system.

IV. CONCLUSION

In summary, we have synthesized single crystals of ZrTe_{3-x} using the isothermal chemical vapor transport method. Magnetization, specific heat, and transport measurements were conducted on a crystal, revealing bulk anisotropic type-II superconductivity at a temperature of 3.59(4) K. The observation of an isotropic s-wave superconducting gap further classifies the compound as a weakly coupled conventional superconductor. More importantly, the presence of a quasi-2D nature is confirmed by angle-dependent upper critical field measurements conforming to the 2D Tinkham model and observation of the BKT transition at 2.91(1) K. Our results suggest that the introduction of Te vacancies can be used as an effective tuning parameter to modulate the balance between superconductivity and the charge density wave transition. This approach not only uncovers the relation between these competing ground states, but also offers an opportunity to explore numerous low-dimensional quantum phases in bulk materials of group IVB TMTCS, considerably broadening the new pathway for pursuing two-dimensional superconductivity in layered materials.

V. ACKNOWLEDGMENTS

P. M. acknowledges the funding agency DST-INSPIRE, Government of India, for providing the SRF fellowship. R. P. S. acknowledges the Science and Engineering Research Board, Government of India, for the Core Research Grant CRG/2023/000817.

- [1] G. Ghiringhelli, M. L. Tacon, M. Minola, S. Blanco-Canosa, C. Mazzoli, N. B. Brookes, G. M. D. Luca, A. Frano, D. G. Hawthorn, F. He, T. Loew, M. M. Sala, D. C. Peets, M. Salluzzo, E. Schierle, R. Sutarto, G. A. Sawatzky, E. Weschke, B. Keimer, and L. Braicovich, Long-Range Incommensurate Charge Fluctuations in $(\text{Y}, \text{Nd})\text{Ba}_2\text{Cu}_3\text{O}_{6+x}$, *Science* **337**, 821 (2012).
- [2] T. P. Croft, C. Lester, M. S. Senn, A. Bombardi, and S. M. Hayden, Charge density wave fluctuations in $\text{La}_{2-x}\text{Sr}_x\text{CuO}_4$ and their competition with superconductivity, *Phys. Rev. B* **89**, 224513 (2014).
- [3] K. Kudo, Y. Nishikubo, and M. Nohara, Coexistence of Superconductivity and Charge Density Wave in SrPt_2As_2 , *J. Phys. Soc. Japan* **79**, 123710 (2010).
- [4] G. Grüner, The dynamics of charge-density waves, *Rev. Mod. Phys.* **60**, 1129 (1988).
- [5] A. P. Petrović, D. Ansermet, D. Chernyshov, M. Hoesch, D. Salloum, P. Gougeon, M. Potel, L. Boeri, and C. Panagopoulos, A disorder-enhanced quasi-one-dimensional superconductor, *Nat. commun.* **7**, 12262 (2016).
- [6] M. Hoesch, L. Gannon, K. Shimada, B. J. Parrett, M. D. Watson, T. K. Kim, X. Zhu, and C. Petrović, Disorder

Quenching of the Charge Density Wave in ZrTe_3 , *Phys. Rev. Lett.* **122**, 017601 (2019).

[7] J. Chang, E. Blackburn, A. Holmes, N. B. Christensen, J. Larsen, J. Mesot, R. Liang, D. Bonn, W. Hardy, A. Wanphul, *et al.*, Direct observation of competition between superconductivity and charge density wave order in $\text{YBa}_2\text{Cu}_3\text{O}_{6.67}$, *Nat. Phys.* **8**, 871 (2012).

[8] M. Le Tacon, A. Bosak, S. Souliou, G. Dellea, T. Loew, R. Heid, K. Bohnen, G. Ghiringhelli, M. Krisch, and B. Keimer, Inelastic X-ray scattering in $\text{YBa}_2\text{Cu}_3\text{O}_{6.6}$ reveals giant phonon anomalies and elastic central peak due to charge-density-wave formation, *Nat. Phys.* **10**, 52 (2014).

[9] X. Zhu, W. Ning, L. Li, L. Ling, R. Zhang, J. Zhang, K. Wang, Y. Liu, L. Pi, Y. Ma, H. Du, M. Tian, Y. Sun, C. Petrovic, and Y. Zhang, Superconductivity and charge density wave in $\text{ZrTe}_{3-x}\text{Se}_x$, *Sci. Rep.* **6**, 26974 (2016).

[10] C.-S. Lian, Interplay of charge ordering and superconductivity in two-dimensional 2H group V transition-metal dichalcogenides, *Phys. Rev. B* **107**, 045431 (2023).

[11] A. Patra and C. S. Rout, Anisotropic quasi-one-dimensional layered transition-metal trichalcogenides: synthesis, properties and applications, *RSC Adv.* **10**, 36413 (2020).

[12] H. Wang, C. H. Chan, C. H. Suen, S. P. Lau, and J.-Y. Dai, Magnetotransport Properties of Layered Topological Material ZrTe_2 Thin Film, *ACS Nano* **13**, 6008 (2019), pMID: 31013050.

[13] J. Wang, Y. Wang, M. Wu, J. Li, S. Miao, Q. Hou, Y. Li, J. Zhou, X. Zhu, Y. Xiong, *et al.*, Magnetotransport due to conductivity fluctuations in non-magnetic ZrTe_2 nanoplates, *Appl. Phys. Lett.* **120** (2022).

[14] F. Tang, Y. Ren, P. Wang, R. Zhong, J. Schneeloch, S. A. Yang, K. Yang, P. A. Lee, G. Gu, Z. Qiao, and Z. Liyuan, Three-dimensional quantum Hall effect and metal-insulator transition in ZrTe_5 , *Nat.* **569**, 537 (2019).

[15] H. Wang, H. Liu, Y. Li, Y. Liu, J. Wang, J. Liu, J.-Y. Dai, Y. Wang, L. Li, J. Yan, D. Mandrus, X. C. Xie, and J. Wang, Discovery of log-periodic oscillations in ultraquantum topological materials, *Sci. Adv.* **4**, eaau5096 (2018).

[16] H. Weng, C. Fang, Z. Fang, and X. Dai, Coexistence of Weyl fermion and massless triply degenerate nodal points, *Phys. Rev. B* **94**, 165201 (2016).

[17] A. Bouhon, Q. Wu, R.-J. Slager, H. Weng, O. V. Yazyev, and T. Bzdušek, Non-Abelian reciprocal braiding of Weyl points and its manifestation in ZrTe , *Nat. Phys.* **16**, 1137 (2020).

[18] M. Hoesch, X. Cui, K. Shimada, C. Battaglia, S.-i. Fujimori, and H. Berger, Splitting in the Fermi surface of ZrTe_3 : A surface charge density wave system, *Phys. Rev. B* **80**, 075423 (2009).

[19] K. Yamaya, S. Takayanagi, and S. Tanda, Mixed bulk-filament nature in superconductivity of the charge-density-wave conductor ZrTe_3 , *Phys. Rev. B* **85**, 184513 (2012).

[20] S. L. Gleason, Y. Gim, T. Byrum, A. Kogar, P. Abbamonte, E. Fradkin, G. J. MacDougall, D. J. Van Harlingen, X. Zhu, C. Petrovic, and S. L. Cooper, Structural contributions to the pressure-tuned charge-density-wave to superconductor transition in ZrTe_3 : Raman scattering studies, *Phys. Rev. B* **91**, 155124 (2015).

[21] K. Gu, R. A. Susilo, F. Ke, W. Deng, Y. Wang, L. Zhang, H. Xiao, and B. Chen, Pressure-induced enhancement in the superconductivity of ZrTe_3 , *J. Phys. : Condens. Matter* **30**, 385701 (2018).

[22] L. de Faria, F. Abud, L. Correa, L. Ishikura, M. da Luz, M. Torikachvili, and A. Machado, Superconductivity, antiferromagnetism, and charge density waves in ZrTe_3 intercalated with Terbium, *J. Alloys and Compd.* **1005**, 175919 (2024).

[23] L. M. Ishikura, F. S. A. Abud, L. R. de Faria, K. Mikalajunas, B. B. Canelhas, D. C. Ferreira, M. S. da Luz, M. S. Torikachvili, and A. J. da Silva Machado, Superconductivity and charge density waves in ruthenium intercalated ZrTe_3 , *Phys. Lett. A* **565**, 131145 (2026).

[24] K. Yamaya, M. Yoneda, S. Yasuzuka, Y. Okajima, and S. Tanda, The effect of pressure on the charge-density wave and superconductivity in ZrTe_3 , *J. Phys.: Condens. Matter* **14**, 10767 (2002).

[25] R. Yomo, K. Yamaya, M. Abliz, M. Hedo, and Y. Uwatoko, Pressure effect on competition between charge density wave and superconductivity in ZrTe_3 : Appearance of pressure-induced reentrant superconductivity, *Phys. Rev. B* **71**, 132508 (2005).

[26] J. Wang, M. Wu, W. Zhen, T. Li, Y. Li, X. Zhu, W. Ning, and M. Tian, Superconductivity in single-crystalline ZrTe_{3-x} ($x \leq 0.5$) nanoplates, *Nanoscale Adv.* **5**, 479 (2023).

[27] X. Zhu, H. Lei, and C. Petrovic, Coexistence of Bulk Superconductivity and Charge Density Wave in Cu_xZrTe_3 , *Phys. Rev. Lett.* **106**, 246404 (2011).

[28] H. Lei, X. Zhu, and C. Petrovic, Raising T_c in charge density wave superconductor ZrTe_3 by Ni intercalation, *Europhys. Lett.* **95**, 17011 (2011).

[29] C. Patra, T. Agarwal, Arushi, P. Manna, N. Bhatt, R. S. Singh, and R. P. Singh, Superconducting Properties of Layered Chalcogenides 1T-RhSeTe, *Adv. Quantum Technol.* **7**, 2400175 (2024).

[30] C. Patra, T. Agarwal, S. Srivastava, R. R. Chowdhury, M. Saravanan, and R. P. Singh, Planar Hall Effect and Quasi-2D Anisotropic Superconductivity in Topological Candidate 1T-NbSeTe, *Adv. Quantum Technol.* **7**, 2300448 (2024).

[31] X. Zhu, B. Lv, F. Wei, Y. Xue, B. Lorenz, L. Deng, Y. Sun, and C.-W. Chu, Disorder-induced bulk superconductivity in ZrTe_3 single crystals via growth control, *Phys. Rev. B* **87**, 024508 (2013).

[32] P. Manna, S. Sharma, T. Agarwal, S. Srivastava, P. Mishra, and R. Singh, Quasi-two-dimensional superconductivity in 1T-Ti_{1-x}Ta_xSe₂, *arXiv:2511.00605* (2025).

[33] T. Agarwal, C. Patra, A. Kataria, R. R. Chowdhury, and R. Singh, Quasi-two-dimensional anisotropic superconductivity in Li-intercalated 2H-TaS₂, *Phys. Rev. B* **107**, 174509 (2023).

[34] K. Momma and F. Izumi, VESTA 3 for three-dimensional visualization of crystal, volumetric and morphology data, *J. Appl. Cryst.* **44**, 1272 (2011).

[35] J. Rodríguez-Carvajal, Recent advances in magnetic structure determination by neutron powder diffraction, *Physica B: Condens. Matter* **192**, 55 (1993).

[36] See supplemental material for additional details on powder XRD data, EDAX data, magnetization, resistivity, and Uemura plot, which includes refs. [46-58].

[37] B. S. Chandrasekhar, A note on the maximum critical field of high-field superconductors, *Appl. Phys. Lett.* **1**, 7 (1962).

[38] A. M. Clogston, Upper Limit for the Critical Field in Hard Superconductors, *Phys. Rev. Lett.* **9**, 266 (1962).

[39] N. R. Werthamer, E. Helfand, and P. C. Hohenberg, Temperature and Purity Dependence of the Superconducting

Critical Field, H_{c2} . III. Electron Spin and Spin-Orbit Effects, *Phys. Rev.* **147**, 295 (1966).

[40] E. Helfand and N. R. Werthamer, Temperature and Purity Dependence of the Superconducting Critical Field, H_{c2} . II, *Phys. Rev.* **147**, 288 (1966).

[41] T. Palstra, B. Batlogg, L. Schneemeyer, R. Van Dover, and J. V. Waszczak, Angular dependence of the upper critical field of $\text{Bi}_{2.2}\text{Sr}_2\text{Ca}_{0.8}\text{Cu}_2\text{O}_{8+\delta}$, *Phys. Rev. B* **38**, 5102 (1988).

[42] W. L. McMillan, Transition Temperature of Strong-Coupled Superconductors, *Phys. Rev.* **167**, 331 (1968).

[43] H. Padamsee, J. Neighbor, and C. Shiffman, Quasiparticle phenomenology for thermodynamics of strong-coupling superconductors, *J. Low Temp. Phys.* **12**, 387 (1973).

[44] K. Takiguchi, Y. Krockenberger, Y. Taniyasu, and H. Yamamoto, Berezinskii-Kosterlitz-Thouless transition in rhenium nitride films, *Phys. Rev. B* **110**, 024516 (2024).

[45] G. Venditti, J. Biscaras, S. Hurand, N. Bergeal, J. Lesueur, A. Dogra, R. C. Budhani, M. Mondal, J. Jesudasan, P. Raychaudhuri, S. Caprara, and L. Benfatto, Nonlinear $I-V$ characteristics of two-dimensional superconductors: Berezinskii-Kosterlitz-Thouless physics versus inhomogeneity, *Phys. Rev. B* **100**, 064506 (2019).

[46] Y. J. Uemura, G. M. Luke, B. J. Sternlieb, J. H. Brewer, J. F. Carolan, W. N. Hardy, R. Kadono, J. R. Kempton, R. F. Kiefl, S. R. Kreitzman, P. Mulhern, T. M. Riseman, D. L. Williams, B. X. Yang, S. Uchida, H. Takagi, J. Gopalakrishnan, A. W. Sleight, M. A. Subramanian, C. L. Chien, M. Z. Cieplak, G. Xiao, V. Y. Lee, B. W. Statt, C. E. Stronach, W. J. Kossler, and X. H. Yu, Universal Correlations between T_c and $\frac{n_s}{m^*}$ (Carrier Density over Effective Mass) in High- T_c Cuprate Superconductors, *Phys. Rev. Lett.* **62**, 2317 (1989).

[47] Z. Wang, J. Yuan, J. Wosnitza, H. Zhou, Y. Huang, K. Jin, F. Zhou, X. Dong, and Z. Zhao, The upper critical field and its anisotropy in $(\text{Li}_{1-x}\text{Fe}_x)\text{OHFe}_{1-y}\text{Se}$, *J. Phys. Condens. Matter* **29**, 025701 (2017).

[48] N. Keller, J. L. Tholence, A. Huxley, and J. Flouquet, Angular Dependence of the Upper Critical Field of the Heavy Fermion Superconductor UPt_3 , *Phys. Rev. Lett.* **73**, 2364 (1994).

[49] C. Patra, T. Agarwal, R. R. Chaudhari, and R. P. Singh, Two-dimensional multigap superconductivity in bulk 2H-TaSeS, *Phys. Rev. B* **106**, 134515 (2022).

[50] J. L. Zhang, L. Jiao, F. F. Balakirev, X. C. Wang, C. Q. Jin, and H. Q. Yuan, Upper critical field and its anisotropy in LiFeAs , *Phys. Rev. B* **83**, 174506 (2011).

[51] N. Kurita, K. Kitagawa, K. Matsubayashi, A. Kismarhardja, E.-S. Choi, J. S. Brooks, Y. Uwatoko, S. Uji, and T. Terashima, Determination of the upper critical field of a single crystal LiFeAs : The magnetic torque study up to 35 Tesla, *J. Phys. Soc. Jpn.* **80**, 013706 (2010).

[52] F. Soto, H. Berger, L. Cabo, C. Carballeira, J. Mosqueira, D. Pavuna, P. Toimil, and F. Vidal, Electric and magnetic characterization of NbSe_2 single crystals: Anisotropic superconducting fluctuations above T_C , *Physica C* **460-462**, 789 (2007).

[53] J. Cheng, J. Bai, B. Ruan, P. Liu, Y. Huang, Q. Dong, Y. Huang, Y. Sun, C. Li, L. Zhang, Q. Liu, W. Zhu, Z. Ren, and G. Chen, Superconductivity in a Layered Cobalt Oxychalcogenide $\text{Na}_2\text{CoSe}_2\text{O}$ with a Triangular Lattice, *J. Am. Chem. Soc.* **146**, 5908 (2024).

[54] N. Keller, J. Brison, P. Lejay, J. Tholence, A. Huxley, L. Schmidt, A. Buzdin, and J. Flouquet, Review on the phase diagram and the upper critical field anisotropy of uranium-based heavy fermion superconductors, *Physica B: Condens. Matter* **206-207**, 568 (1995), proceedings of the International Conference on Strongly Correlated Electron Systems.

[55] E.-W. Scheidt, M. Herzinger, A. Fischer, D. Schmitz, J. Reiners, F. Mayr, F. Loder, M. Baenitz, and W. Scherer, On the nature of superconductivity in the anisotropic dichalcogenide $\text{NbSe}_2\{\text{CoCp}_2\}_x$, *J. Phys. : Condens. Matter* **27**, 155701 (2015).

[56] Y. Yang, S. Fang, V. Fatemi, J. Ruhman, E. Navarro-Moratalla, K. Watanabe, T. Taniguchi, E. Kaxiras, and P. Jarillo-Herrero, Enhanced superconductivity upon weakening of charge density wave transport in 2H-TaS₂ in the two-dimensional limit, *Phys. Rev. B* **98**, 035203 (2018).

[57] M. Abdel-Hafiez, X.-M. Zhao, A. A. Kordyuk, Y.-W. Fang, B. Pan, Z. He, C.-G. Duan, J. Zhao, and X.-J. Chen, Enhancement of superconductivity under pressure and the magnetic phase diagram of tantalum disulfide single crystals, *Sci. Rep.* **6**, 31824 (2016).

[58] G. F. Chen, Z. Li, J. Dong, G. Li, W. Z. Hu, X. D. Zhang, X. H. Song, P. Zheng, N. L. Wang, and J. L. Luo, Transport and anisotropy in single-crystalline SrFe_2As_2 and $A_{0.6}\text{K}_{0.4}\text{Fe}_2\text{As}_2$ ($A = \text{Sr}, \text{Ba}$) superconductors, *Phys. Rev. B* **78**, 224512 (2008).